Contents lists available at ScienceDirect

Spectrochimica Acta Part A:
Molecular and Biomolecular Spectroscopy

journal homepage: www.journals.elsevier.com/spectrochimica-acta-part-a-molecular-and-biomolecular-spectroscopy

Rapid and ultrasensitive detection of acute kidney injury biomarkers CH3L1 and L-FABP using surface-enhanced Raman spectroscopy

Luyao Wang [a], Pei Ma [a,*], Hui Chen [a], Min Chang [a], Ping Lu [a], Nan Chen [b], Xuedian Zhang [a,c], Yanhua Li [d], Mingxing Sui [d,*]

[a] Key Laboratory of Optical Technology and Instrument for Medicine, Ministry of Education, College of Optical-Electrical and Computer Engineering, University of Shanghai for Science and Technology, Shanghai 200093, China
[b] School of Electrical Engineering, Nantong University, Nantong 226019, China
[c] Shanghai Institute of Intelligent Science and Technology, Tongji University, Shanghai 200092, China
[d] Department of Organ Transplantation, Shanghai Changhai Hospital, Shanghai 200433, China

HIGHLIGHTS

- Surface-enhanced Raman spectroscopy (SERS) is employed to characterize two important acute kidney injury (AKI) biomarkers, chitinase 3-like 1 (CH3L1) and liver fatty acid binding protein (L-FABP).
- GO/Au@Ag nanoparticles are used as SERS substrates.
- Trace amount of CH3L1 and L-FABP were detected at levels as low as 1.21×10^{-8} mg/mL and 0.62×10^{-8} mg/mL, respectively.
- The proposed method on multiple biomarker detection will greatly improve the early diagnosis and intervention of AKI.

GRAPHICAL ABSTRACT
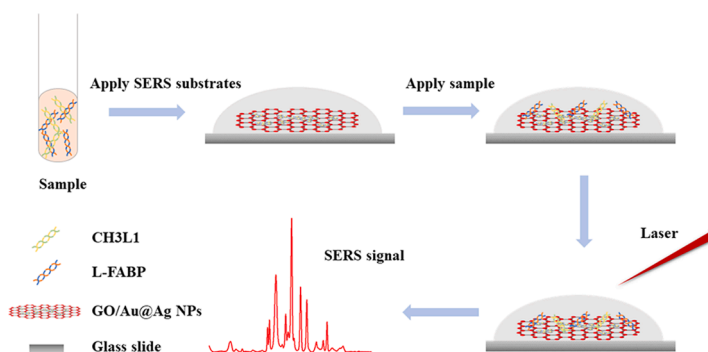
ABSTRACT

Chitinase 3-like 1 (CH3L1) and liver fatty acid binding protein (L-FABP) are promising biomarkers for the early diagnosis of acute kidney injury (AKI). Here, a highly sensitive method for the quantitative detection of CH3L1 and L-FABP by surface-enhanced Raman spectroscopy (SERS) based on graphene oxide/gold and silver core–shell nanoparticles (GO/Au@Ag NPs) was proposed. The results showed that such GO/Au@Ag substrate can achieve rapid sensing of CH3L1 and L-FABP with a wide response range (2×10^{-1} to 2×10^{-8} mg/mL and 1.2×10^{-1} to 1.2×10^{-8} mg/mL, respectively) and high sensitivity. The detection limits of CH3L1 and L-FABP were 1.21×10^{-8} mg/mL and 0.62×10^{-8} mg/mL, respectively. In addition, the simultaneous detection of the two biomarkers in serum was demonstrated, showing the feasibility of this method in the complex biological environment. The detection of CH3L1 and L-FABP will greatly improve the early diagnosis and intervention of AKI.

* Corresponding authors.
  E-mail addresses: peima@usst.edu.cn (P. Ma), mingxingsui@smmu.edu.cn (M. Sui).
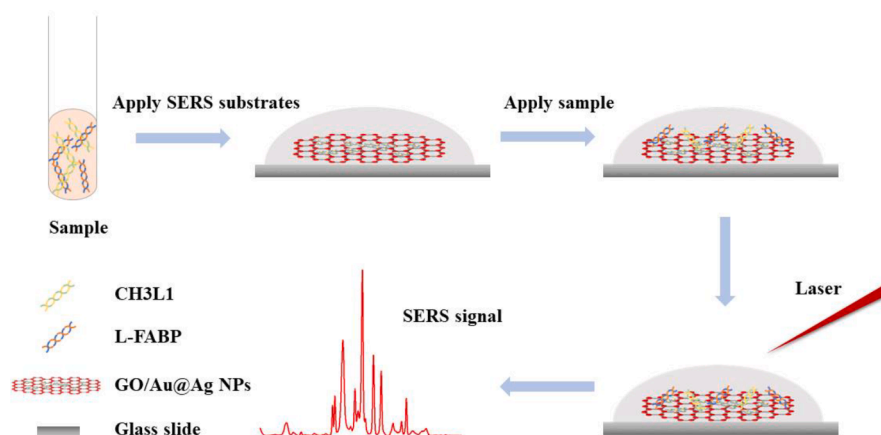
Fig. 1. The schematic diagram of the SERS detection of AKI biomarkers.

1. Introduction

Acute kidney injury (AKI) is a common problem in the contemporary practice of medicine and urology. It is frequently associated with severe clinical outcomes, including chronic kidney diseases, and cardiovascular diseases. AKI occurs in approximately 10–15% of hospitalized patients and has been reported to have a prevalence of up to 50% in intensive care[1]. It is also associated with high morbidity and mortality[2]. AKI occurs as a result of sudden impairment of renal function due to a wide range of pathogenic factors[3]. It is presented with reduced urine volume, severe metabolic disorders, and could even require renal replacement therapy if delayed diagnosed[4]. Current clinical indicators for estimating renal function, serum creatinine, urine volume, etc., only become measurable after significant kidney function loss, and after sufficient time of the function loss[5–8]. Other tracers, such as inulin and iothalamate, and are cumbersome to perform[9]. AKI can be cured or improved only when it is diagnosed early, thus early diagnosis and timely intervention is the key to treatment and improvement of the condition[10]. Recent studies found new biomarkers that may be superior to the current methods in the early diagnosis and assessment of AKI, such as, neutrophil gelatinase-associated lipid carrier protein (NGAL), kidney injury molecule-1 (KIM-1), interleukin 18 (IL-18), Chitinase 3-like 1 (CH3L1) and liver fatty acid binding protein (L-FABP) [11–14].

CH3L1, an emerging biomarker for AKI, is a 40 kDa mammalian glycoprotein that mediates inflammation, apoptosis, and macrophage polarization. [15–18]. CHI3L1 is secreted by macrophages activated in the kidney in response to stress or injury. It was shown that the degree of renal injury was directly correlated with CHI3L1 expression in the kidney and the level of CHI3L1 in urine[19,20]. L-FABP is a newly discovered biomarker for early diagnosis of acute diseases[13,21]. It has been reported that in AKI, urinary levels of the L-FABP increased earlier than serum creatinine in patients [22–25]. It is worth noting that there is no near-perfect biomarker due to the heterogeneous etiology of AKI and each identified biomarker has strengths and weaknesses. The simultaneous detection of multiple biomarkers can greatly help the early and accurate diagnosis of AKI.

To date, many different methods have been reported to detect protein-like biomarkers, including enzyme-linked immunosorbent assay [26], chemiluminescence immunoassay[27], electrochemical immunosensor[28], fluorescence immunoassay[29], light scattering immunoassay[30], and radioimmunoassay[31]. However, most of these methods are limited by processing time, complexity, or poor sensitivity. Rapid, simple, highly-sensitive, and cost-effective detection techniques are in urgent need. As a label-free technique, surface-enhanced Raman spectroscopy (SERS) is considered to be a powerful tool for evaluating complex chemical reactions and biological analysis due to its high sensitivity[32,33], selectivity[34,35] and good biocompatibility [36–38]. For example, Abramczyk, H., et al. used unlabeled Raman spectroscopy to detect spectral changes that arise in proteins due to phosphorylation in the tissue of human breasts, small intestines, and brain tumors, as well as in the normal human astrocytes and primary glioblastoma U-87 MG cell lines [39]. Liu et al. used gold nanoprobes to perform Raman imaging of microRNA-21 and telomerase in living cells, providing potential tools for cancer diagnosis and progression monitoring[40]. More importantly, SERS can present the characteristic peaks of many substances in a single spectrum. This made SERS ideal for measuring multiple biomarkers simultaneously.

In recent years, composite structures of graphene and metal nanoparticles have been proposed to improve the reproducibility of SERS substrates. It has been reported that graphene substrates can be chemically enhanced to effectively enhance the Raman signal of analytes[41]. Meanwhile, GO, a derivative of graphene, is functionalized by abundant oxygen groups with good biocompatibility and can be used as an active site for further modifications[42]. More interestingly, the graphene oxide/metal nanoparticle composite structure is highly compatible with biomolecules through dispersion interactions and electrostatic interactions, etc., which facilitates the surface enrichment of proteins and thus localization at hot spots[43]. These features make graphene oxide and metal nanoparticle hybrids promising as SERS active substrates for sensitive and stable biomolecular detection.

In this study, SERS was used to detect biomarkers CH3L1 and L-FABP for the early indication of AKI. The overview of this method is illustrated in Fig. 1. GO/Au@Ag core/shell nanoparticles were synthesized as the SERS substrate. The characteristic peaks of CH3L1 at 997 cm^{-1} and L-FABP at 1161 cm^{-1} were selected for quantitative analysis, with the concentration range of 2×10^{-1} to 2×10^{-8} mg/mL and 1.2×10^{-1} to 1.2×10^{-8} mg/mL, respectively. The responses showed ideal linearity in wide concentration ranges, demonstrating that SERS based on the GO/Au@Ag core–shell structure was a sensitive and reliable method for the detection of CH3L1 and L-FABP. In addition, the simultaneous detection of both biomarkers in serum has demonstrated the feasibility of this method in the real biological environment. This method is highly-sensitive and easy-to-operate, and is expected to greatly help with the early diagnosis of AKI, as well as a variety of other medical diagnostic applications.

2. Materials and methods

2.1. Materials and reagents

All chemicals and reagents were analytically grade, and all experiments used deionized water (18.25 MΩ). Fetal bovine serum (FBS, 10%) was obtained from Hangzhou Sijiqing Biological Engineering Materials

Co., Ltd. TRIS hydrochloride (Tris-HCL,0.1 M, PH8.0, RNase free) was obtained from Qingdao Jieshikang Biotechnology Co., Chloroauric acid tetrahydrate (HAuCl$_4$·3H$_2$O), sodium citrate dihydrate (C$_6$H$_5$Na$_3$O$_7$·2H$_2$O $\geq$ 99.0%), sodium d-gluconate (C$_6$H$_{11}$NaO$_7$, $\geq$99.0%), silver nitrate (AgNO$_3$), sodium hydroxide (NaOH), are all provided by Shanghai Macklin Biochemical Technology Co., Ltd. Graphene oxide (GO) dispersion solution (5 mg/mL) was supplied by the XF Nano, Inc. CH3L1 (2 mg/mL) and L-FABP (1.2 mg/mL) proteins were provided by Changhai hospital and analyzed by Wuhan Seville Biotechnology Co., Ltd. Rhodamine B (RB) is provided by Tianjin Guangfu Fine Chemical Research Institute.

2.2. Synthesis and characterization of GO/Au@Ag nanoparticles

The preparation of GO/Au-Ag core–shell nanostructures (GO/Au@Ag NPs) can be divided into two steps. First, Au NPs were prepared by reducing HAuCl4·3H$_2$O mediated with sodium citrate dihydrate [44]. 306 μL HAuCl$_4$·3H$_2$O (10% w/w) was dissolved in 99.694 mL deionized water, and the mixture was heated to boiling. Then, 10 mL of sodium citrate dihydrate (1% w/w) was added to the boiling mixture. Continue to heat for 15 min until it turns wine red, cool to room temperature. Then Ag was covered on the surface of Au NPs by the reduction of AgNO$_3$ by D(+)-glucose. 6 mL of the resulting gold NPs was centrifuged at a speed of 9500 r/min for 35 min. The sediment after removing the supernatant was diluted back to 6 mL, and 54 mL deionized water was added, followed by stirring and heating to 60℃. 500 μL of 0.08 M D (+) Glucose solution and 140 μL of 0.1 M AgNO$_3$ solution were then added, followed by 200 μL of 1 M NaOH solution. Heat the mixture for 30 min, until the solution was orange-yellow, cool to room temperature and keep in the dark one week for later use. Next, 10 mL of aqueous GO solution (0.01 mg/mL) was added to 30 mL of Au@Ag NPs colloid, sonicated for 3 min, and stirred continuously for 2 h to mix thoroughly. The Au@Ag and GO/Au@Ag nanoparticles were characterized by an Evolution 350 UV–vis (Thermo Scientific, China) in the wavelength range of 300–800 nm. The GO/Au@Ag nanoparticles size distribution was measured by the dynamic light scattering experiments (Zetasizer, Nano-ZS90, Malvern, UK). The surface morphology and the size of the GO/Au@Ag nanoparticles were characterized by a JEM-2100F (JEOL, Japan) high-resolution transmission electron microscope (TEM) at an acceleration voltage of 200 kV. In order to exclude the influence of substrates on Raman signals, the Raman spectrum of blank SERS substrates was measured. Then the enhancement effect of Au@Ag NPs was compared with that of GO/Au@Ag NPs by measuring Rhodamine B (RB) at a concentration of 10^{-2} mM.

2.3. CH3L1 and L-FABP standard solution preparation and SERS detection

CH3L1 and L-FABP standard solutions were prepared for the SERS measurement. According to previous studies, urine CH3L1 was usually not detectable when lower than 0.2 ng/mL in healthy humans, with 5 ng/mL being used as the baseline[45,46]. The baseline for L-FABP is 10.1 ng/mL[47], and the concentration of the biomarker was usually higher than normal in patients with acute kidney injury[48].

The initial concentrations of CH3L1 and L-FABP were 2 mg/mL and 1.2 mg/mL, respectively, and were then diluted with Tris-HCL to obtain CH3L1 standard samples with concentrations of 2 × 10^{-1}, 2 × 10^{-2}, 2 × 10^{-3}, 2 × 10^{-4}, 2 × 10^{-5}, 2 × 10^{-6}, 2 × 10^{-7}, 2 × 10^{-8} mg/mL and L-FABP standard samples with concentrations of 1.2 × 10^{-1}, 1.2 × 10^{-2}, 1.2 × 10^{-3}, 1.2 × 10^{-4}, 1.2 × 10^{-5}, 1.2 × 10^{-6}, 1.2 × 10^{-7}, 1.2 × 10^{-8} mg/mL, respectively. For each sample, 2 μL of GO/Au@Ag nanocomposites was added dropwise to the glass slide, and 2 μL of standard sample was added dropwise after for a few moments, followed by SERS detection. eight SERS spectra from random positions were measured to obtain an average spectrum.

2.4. Real sample pre-treatment and SERS detection

In the experiment, the fetal bovine serum (FBS) was first diluted with Tris-HCL (dilutions of 1:9), and then CH3L1 and L-FABP with different concentrations were added respectively. In order to ensure that FBS would not interfere with SERS detection of biomarkers, the SERS spectrum of FBS (10%) was measured using GO/Au@Ag nanoparticles. The concentrations of CH3L1 serum samples were made to be 2 × 10^{-1}, 2 × 10^{-2}, 2 × 10^{-3}, 2 × 10^{-4}, 2 × 10^{-5}, 2 × 10^{-6}, 2 × 10^{-7}, 2 × 10^{-8} mg/mL, and the concentrations of L-FABP serum samples were made to be 1.2 × 10^{-1}, 1.2 × 10^{-2}, 1.2 × 10^{-3}, 1.2 × 10^{-4}, 1.2 × 10^{-5}, 1.2 × 10^{-6}, 1.2 × 10^{-7}, 1.2 × 10^{-8} mg/mL. In addition, serum samples of CH3L1 and L-FABP were mixed to obtain three different concentrations of mixed serum samples for the simultaneous measurement of CH3L1 and L-FABP. The concentrations of CH3L1 in the mixed samples were 1 × 10^{-1}, 1 × 10^{-4} and 1 × 10^{-7} mg/mL and the concentrations of L-FABP were 0.6 × 10^{-1}, 0.6 × 10^{-4} and 0.6 × 10^{-7} mg/mL, respectively (denoted as sample 10^{-1} mg/mL, 10^{-4} mg/mL, 10^{-7} mg/mL).

The SERS assay of serum samples was performed according to the previously mentioned SERS assay for biomarkers. Each spectrum was likewise obtained by averaging the spectra measured at eight random locations.

2.5. Data acquisition and analysis

SERS spectra were collected by a microscopic Raman spectrometer (LabRAM Xplora Plus, HORIBA Scientific, France) under 638 nm excitation. The scattered light from the sample was collected with a 10x objective lens. All spectra were recorded from 400 to 1800 cm^{-1} with a spectral resolution of 1 cm^{-1}.

The acquired Raman and SERS spectra were pre-processed with smoothing, denoising and baseline correction in the commercial software LabSpec6. The optimized SERS spectra were analyzed for correlation between the intensity of the characteristic peaks and the concentration of the analytes. Linear relationships were established between the logarithm of the Raman characteristic peak intensities of the AKI biomarkers CH3L1 and L-FABP and the logarithm of the concentrations of CH3L1 and L-FABP in the samples, respectively. When the concentration range of the sample is large, the linear relationship between the logarithm of the peak intensities (log I) and the logarithm of the sample concentration (log C) is usually adopted[49–51]. The average intensity of the spectra was obtained by eight repeated measurements and the error bar gave the standard deviation (SD) of these eight I value under a certain concentration of sample. The linearity was evaluated by R^2 and a recovery experiment was performed with measurements from CH3L1 and L-FABP in serum sample to verify the prediction accuracy of the established linear calibration model. Limit of detection (LOD) was calculated by definition as three times the value of the instrumental background signal generated by the matrix blank (S/N = 3), as described in the literature[52].

2.6. SERS repeatability measurements

To verify the reproducibility of the SERS signal, a 10^{-2} mM Rhodamine B (RB) solution was mixed with GO/Au@Ag NPs at a volume ratio of 1:1, after which a 50 μm × 50 μm area of the mixed solution (step size 10 μm) was mapped and SERS spectra were record the analyzed.

3. Results and discussion

3.1. Characterization of GO/Au@Ag NPs

GO/Au@Ag NPs were prepared according to a previous reported method, which were then characterized with UV–Vis spectrometer, TEM and dynamic light scattering. The GO/Au@Ag nanoparticles were characterized by an Evolution 350 UV–vis spectrophotometer. As shown
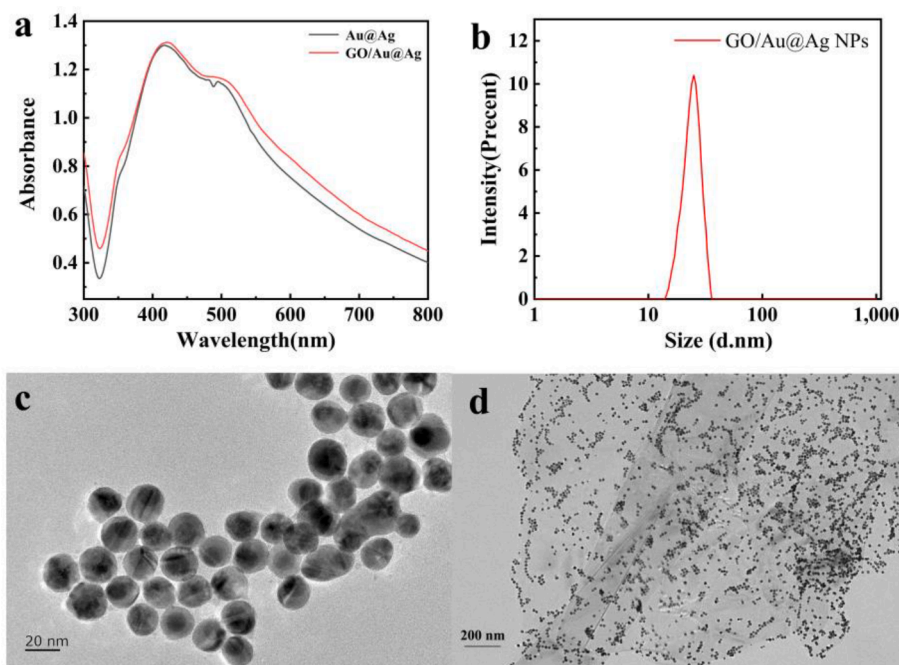
Fig. 2. (a) UV–vis absorption spectra. (b) The particle size distribution of the gold colloid. (c, d) The TEM images of Au@Ag NPs and GO/Au@Ag NPs.
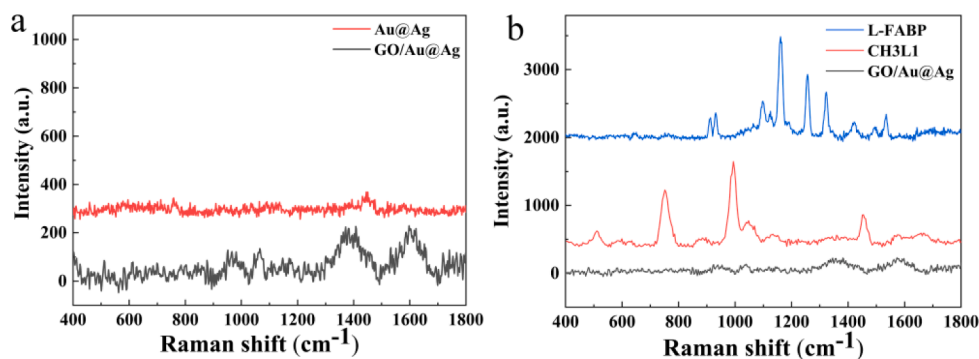

Fig. 3. (a) Spectra of the Au@Ag NPs and GO/Au@Ag NPs. (b) Spectra of the GO/Au@Ag NPs and SERS spectra of the CH3L1 and L-FABP standard solutions at a concentration of 10^{-8} mg/mL.

in Fig.2A, a peak at 411 nm and the shoulder at 520 nm corresponded to silver shell and gold core, which were consistent with the UV–VIS absorption peaks of Ag and Au, respectively. The size distribution was obtained by the dynamic light scattering experiments. Fig. 2B showed that GO/Au@Ag NPs possessed good particle size uniformity. The surface morphology and the size of the GO/Au@Ag nanoparticles were further characterized by TEM. According to TEM images in Fig. 2C, D, the average particle size of GO/Au@Ag NPs is 24 nm. The core–shell structure was clearly observed in Fig. 2C. The nanoparticles were uniformly spread on the GO, as shown in Fig. 2D. It was concluded that the GO/Au@Ag NPs were synthesized with satisfying uniformity.

Raman spectra of blank SERS substrates (Au@Ag NPs and GO/Au@Ag NPs) were measured to investigate possible background signal interference caused by the substrates. From Fig. 3A, it can be observed that Au@Ag did not show any obvious peaks. GO/Au@Ag NPs has two distinct characteristic peaks at around 1355 cm^{-1} and 1600 cm^{-1} due to the D band and the G band. However, the characteristic peaks presented low signal strength with gentle slopes[53–56]. Also, these peaks were not as obvious when compared with the significant characteristic peaks of CH3L1 and L-FABP, even at low concentrations (10^{-8} mg/mL), as shown in Fig. 3B. The SERS properties of GO/Au@Ag hybrid materials
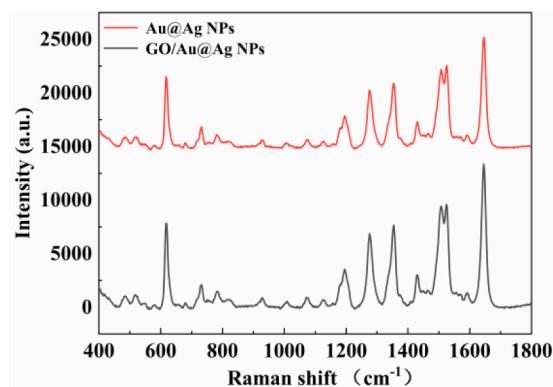

Fig. 4. Average SERS spectra of 10^{-2} mM RB aqueous solution in the presence of GO/Au@Ag NPs and Au@Ag NPs.

and Au@Ag composite nanoparticles alone were then compared. The gold content in both hybrids was adjusted to be the same according to the absorbance of gold nanoparticles. Then 10^{-2} mM Rhodamine B (RB)
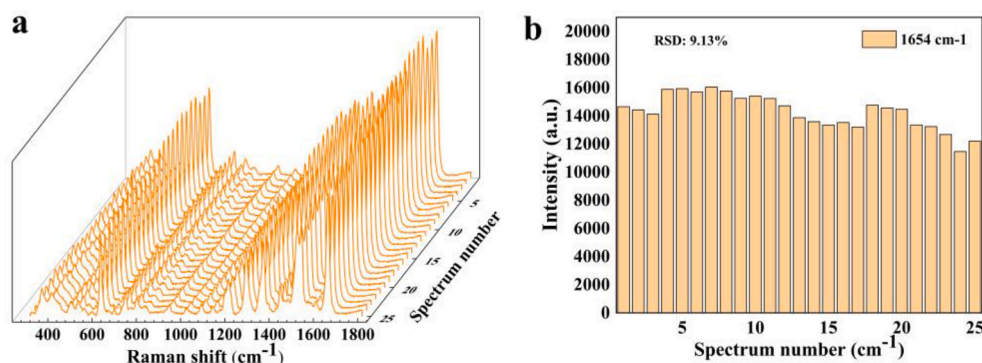
Fig. 5. (a) SERS spectra for all pixels in mapping results. (b) The bar graph of SERS intensity of RB at 1654 cm^{-1} band (RSD of the intensities of 1654 cm^{-1} band is calculated to be 9.13%).
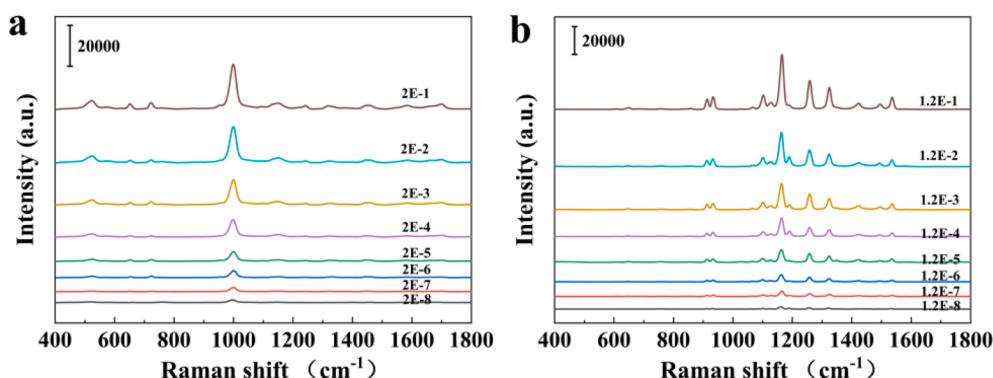

Fig. 6. SERS spectra of the CH3L1 (a) and L-FABP (b) standard solution of eight concentrations shown in different colors.

Table 1
Assignments to SERS spectral peaks of CH3L1 and L-FABP.

Analyte	Peak positions (cm^{-1})	Tentative assignments
CH3L1	518	s-s vibrations
	575	phosphatidylinositol
	756	Ring breathing mode Typtophan
	997	νs (C—C)
	1144	C—N stretch
	1456	δ (C—H)
	1694	ν (C=C)
L-FABP	644	ν (C—S)
	911	CC skeletal stretching
	932	ν (C—C)/ C–H bending
	1098	ring breathing mode
	1161	C–H bending tyrosine
	1254	Proteins: Amide III
	1321	CH3CH2 wagging
	1419	CH2 scissoring
	1491	CN stretching vibration
	1533	Tryptophan: C = C stretching mode

3.2. SERS measurement and analysis of CH3L1 and L-FABP standard solutions

SERS measurement for standard samples was performed and SERS spectra of CH3L1 (2×10^{-1} to 2×10^{-8} mg/mL, corresponds to 3.38×10^{-6} to 3.37×10^{-13} M) and L-FABP (1.2×10^{-1} to 1.2×10^{-8} mg/mL, corresponds to 2.93×10^{-6} to 2.93×10^{-13} M) were shown in Fig. 6. The quantitative performance of this method was investigated based on the SERS intensity at certain characteristic peaks.

The characteristic peaks of CH3L1 at 997 cm^{-1} and L-FABP at 1161, 1254 and 1321 cm^{-1} were clearly observed in all the SERS spectra of CH3L1 and L-FABP standard samples, even at the lowest concentration at 2×10^{-8} mg/mL and 1.2×10^{-8} mg/mL. The characteristic peak assignments of CH3L1 and L-FABP were listed in Table 1. With the increase of biomarker concentration, GO/Au@Ag NPs caused different degrees of enhancement of Raman signals. This is due to the formation of hot spots between the GO/Au@Ag NPs, and the results indicate that the hot spot response SERS signals were extremely sensitive for the detection of biomarkers.

Several characteristic peaks demonstrated the potential in quantitative analysis. For CH3L1, the logarithm of the intensities (log I) at 997 cm^{-1} showed an ideal linear relationship with the logarithm of the concentrations (log C) of the entire measured range, 2×10^{-1} to 2×10^{-8} mg/mL (3.38×10^{-6} to 3.38×10^{-13} M), as shown in Fig. 7. For L-FABP, the log I at the characteristic peaks 1161, 1254 and 1321 cm^{-1} showed satisfying linear relationships with the log C of from the entire range, 1.2×10^{-1} to 1.2×10^{-8} mg/mL (2.93×10^{-6} to 2.93×10^{-13} M), with the highest R^2 value at 1161 cm^{-1}. Based on these results, the limit of detection (LOD) for CH3L1 and L-FABP was calculated to be 1.21×10^{-8} mg/mL and 0.62×10^{-8} mg/mL, respectively, with the 3σ/s method [57]. The linear regression based on logarithm values is often used in SERS when the measured concentration range was large as long as the
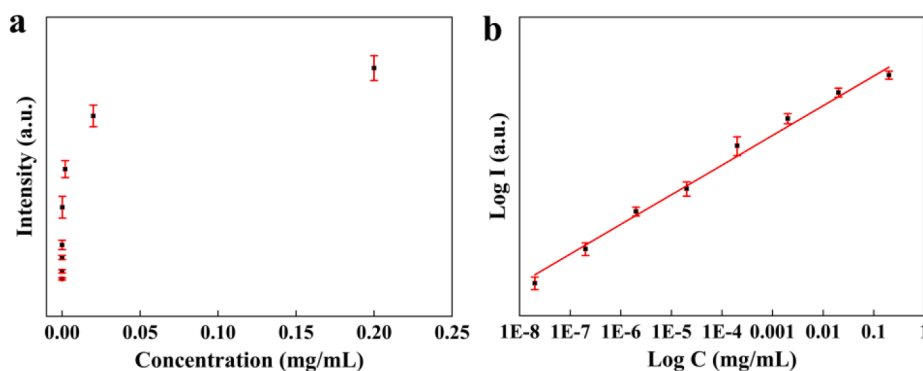
was detected using GO/Au@Ag nanoparticles and Au@Ag nanoparticles as SERS substrates, respectively. The enhanced SERS signal of GO/Au@Ag nanoparticles was superior to that of Au@Ag nanoparticles, as shown in Fig. 4.

In addition, to verify the stability of GO/Au@Ag NPs in SERS, mapping of 10^{-2} mM RB was performed, and the intensity of the characteristic peak at 1645 cm^{-1} of RB was used to generate a SERS mapping image. A 50 μm × 50 μm area in the position on the slide was randomly selected for the experiment. As shown in Fig. 5 below, there was no significant difference in the SERS intensity in the pixels with relative standard deviation (RSD) 9.13%. In conclusion, GO/Au@Ag NPs have satisfactory stability and uniformity in SERS performance.

Fig. 7. Linear relationship established for CH3L1 standard solution. Relationships of intensities of the SERS characteristic peak at 997 cm^{-1} and concentrations of CH3L1 shown in linear coordinates (a) and log coordinates (b).
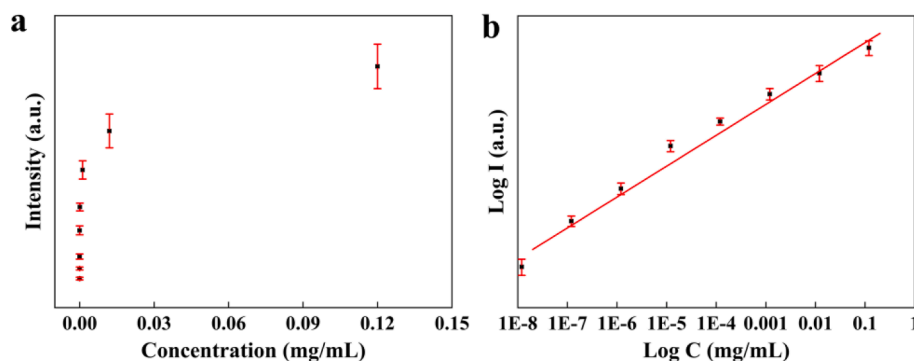

Fig. 8. Linear relationship established for L-FABP standard solution. Relationships of intensities of the SERS characteristic peak at 1161 cm^{-1} and concentrations of L-FABP shown in linear coordinates (a) and log coordinates (b).

Table 2
Linear relationship between concentrations of CH3L1, L-FABP standard solution and Raman intensities at 997, 1161, 1254 and 1321 cm^{-1}.

Analyte	Peaks(cm^{-1})	Linear equation	R^2
CH3L1	997	y = 4.49 + 0.180x	0.98
L-FABP	1161	y = 4.72 + 0.165x	0.98
	1254	y = 4.41 + 0.172x	0.97
	1321	y = 4.44 + 0.183x	0.97

adsorption of analyte molecules followed the Langmuir isotherm [49–51]. Fig. 8 showed the results of the linear fit between the intensity of the characteristic peak at 1161 cm^{-1} and the concentration. The values and error bars in (a) and (b) were averaged intensities and the standard deviations calculated based on eight independent measurements. The linear fitting equations for the four characteristic peaks were presented in Table 2.

In our work, to quantify CH3L1 and L-FABP, the band intensities of 997 cm^{-1} attributed to νs(C–C) and Phenylalanine [58,59] and 1161 cm^{-1} attributed to C–H bending tyrosine[60,61] were extracted to characterize the trends, respectively. These two characteristic peaks are relatively obvious and easy to distinguish, where the biomarkers could be detected at very low concentrations (2 × 10^{-8} mg/mL, 1.2 × 10^{-8} mg/mL) with linear ranges of 2 × 10^{-1} to 2 × 10^{-8} mg/mL and 1.2 × 10^{-1} to 1.2 × 10^{-8} mg/mL, respectively.

3.3. SERS measurement and analysis of CH3L1 and L-FABP in serum sample

To determine the application of the SERS method in the determination of CH3L1 and L-FABP in the real complex environment of serum samples, we examined both biomarkers in fetal bovine serum (FBS,
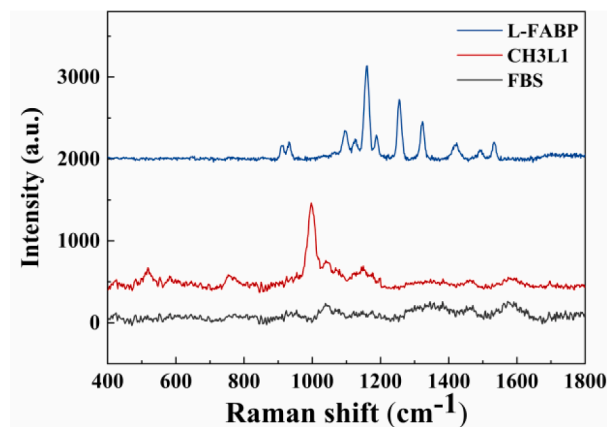

Fig. 9. SERS spectra of FBS, CH3L1 and L-FABP at a concentration of 10^{-8} mg/mL in FBS.

10%) solutions. To make sure FBS does not interfere with SERS detection of the biomarkers, SERS spectrum of FBS (10%) using GO/Au@Ag nanoparticles was measured and the results were shown in Fig. 9. Several characteristic bands at 1021 cm^{-1} and 1453 cm^{-1} can be observed in the SERS spectrum of FBS, which can be attributed to Phe ν_{18a}/C–N stretch and δ(CH)[62,63]. The intensity of these bands was very weak and meanwhile not overlapped with characteristic bands of CH3L1 or L-FABP. The SERS spectra of serum samples exhibited a similar trend to the CH3L1 and L-FABP standard solutions (Fig. 10). which. Similar to the standard solutions, satisfactory linear fitting was acquired at the characteristic peaks 997 and 1161 cm^{-1}, respectively.

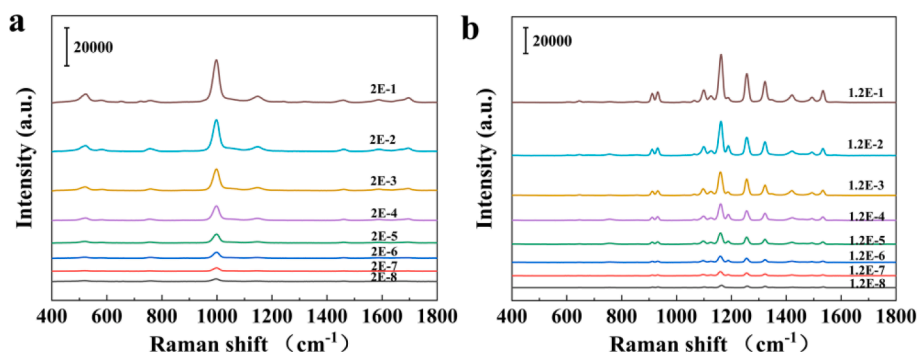At the characteristic peak 997 cm^{-1} of CH3L1, the SERS spectral

Fig. 10. SERS spectra of the CH3L1 (a) and L-FABP (b) serum samples of eight concentrations shown in different colors.
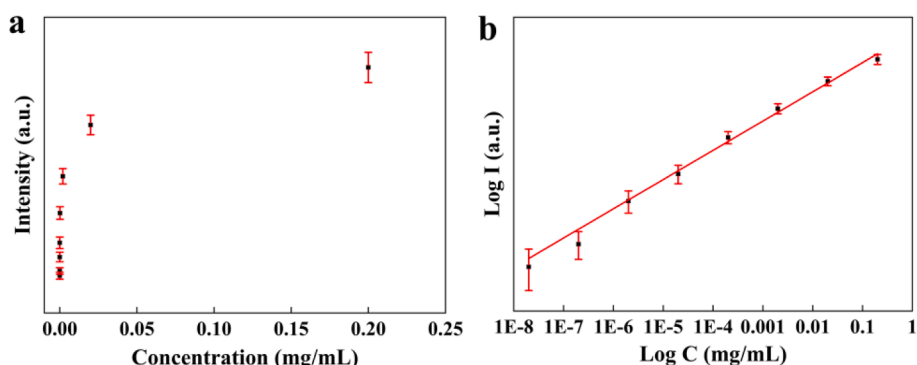

Fig. 11. Linear relationship established for CH3L1 serum samples. Relationships of intensities of the SERS characteristic peak at 997 cm^{-1} and concentrations of CH3L1 shown in linear coordinates (a) and log coordinates (b).
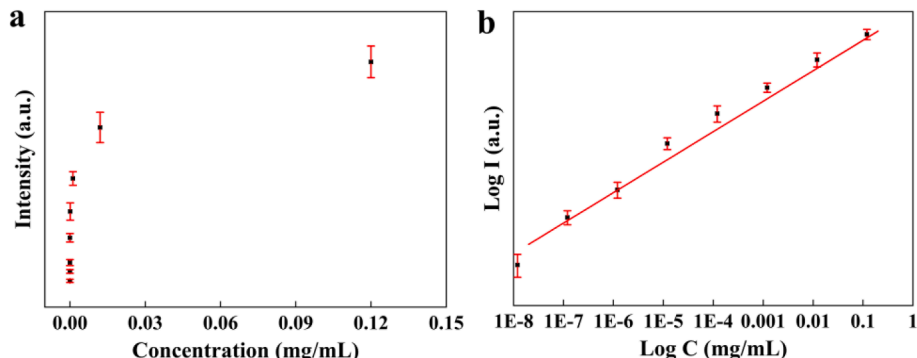

Fig. 12. Linear relationship established for L-FABP serum samples. Relationships of intensities of the SERS characteristic peak at 1161 cm^{-1} and concentrations of L-FABP shown in linear coordinates (a) and log coordinates (b).

Table 3
Linear relationship between concentrations of CH3L1, L-FABP serum samples and SERS intensities at 997, 1161, 1254 and 1321 cm^{-1}.

Analyte	Peaks (cm^{-1})	Linear equation	R^2
CH3L1	997	y = 4.51 + 0.174x	0.97
L-FABP	1161	y = 4.71 + 0.176x	0.98
	1254	y = 4.55 + 0.183x	0.97
	1321	y = 4.35 + 0.176x	0.96

intensity showed a good linear relationship with the concentration of CH3L1 in the range 2×10^{-1} to 2×10^{-8} mg/mL, and the linear fitting between log C and log I was shown in Fig. 11. For the L-FABP serum sample, the SERS spectral intensity showed a good linear relationship with the sample concentration in the range 1.2×10^{-1} to 1.2×10^{-8} mg/mL at the characteristic peak 1161 cm^{-1}, and the linear fitting between

log C and log I was shown in Fig. 12. The values and error bars in (a) and (b) were averaged intensities and the standard deviations calculated based on eight independent measurements. The linear fitting equations for the four characteristic peaks were presented in Table 3.

The results in the serum samples were consistent with those of the standard samples, and the lowest measured concentrations of CH3L1 and L-FABP in the serum samples were 2×10^{-8} mg/mL and 1.2×10^{-8} mg/mL, respectively. The detection limit using this method was lower the baseline for CH3L1 and L-FABP and comparable to the results of previous studies using different techniques[14,45,64–67]. Therefore, we can use this method to analyze the biomarkers qualitatively and quantitatively in real samples and provide a reference value in the screening and early diagnosis of acute kidney injury.

To further evaluate the application of this protocol in real samples, A recovery experiment was performed on a new set of CH3L1 serum samples, and L-FABP serum samples. SERS spectra were acquired and

Table 4

Determination of CH3L1, L-FABP spiked in serum sample.

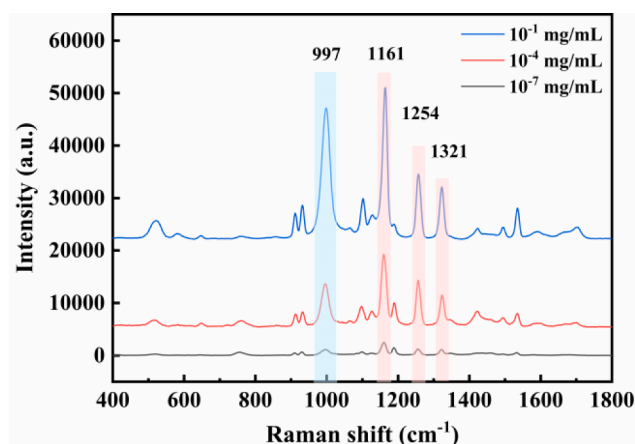| sample	spiked concentration (mg/mL)	detected concentration (mg/mL)	recovery rate (%)
CH3L1	2×10^{-1}	1.971×10^{-1}	98.55
	2×10^{-4}	2.093×10^{-4}	104.65
	2×10^{-7}	1.953×10^{-7}	97.65
L-FABP	1.2×10^{-1}	1.269×10^{-1}	105.83
	1.2×10^{-4}	1.278×10^{-4}	106.58
	1.2×10^{-7}	1.161×10^{-7}	96.83

Fig. 13. Averaged SERS spectra of mixed serum sample (blue shade: the characteristic peak of CH3L1 at 997 cm^{-1}; pink shade: the characteristic peaks of L-FABP at 1161, 1254 and 1321 cm^{-1}).

the intensities at 997 and 1161 cm^{-1} were plugged into the linear regression models to calculated the concentration of each sample. Results were compared to the true values for a calculation of recovery rate (Table 4). The recovery rates were within the acceptable range of 96.83% to 106.58%, literature has reported similar methods and parameters[68,69], indicating that this method has great potential for application in real samples.

3.4. Simultaneous detection of CH3L1 and L-FABP

The SERS spectra of three concentrations of serum samples (mixed sample concentrations of 10^{-1}, 10^{-4}, and 10^{-7} mg/mL) mixed by CH3L1 and L-FABP were shown in Fig. 13. In the mixed solution, the major SERS peaks in all single solutions were still present. The representative characteristic peaks 997, 1161, 1254 and 1321 cm^{-1} were easily observed and can be used to identify the CH3L1 and L-FABP content in the mixture. With increasing biomarker concentration, the SERS characteristic peak intensity also increased. Therefore, it is also feasible to quantitatively determine the content of a biomarker in complex samples with multiple biomarkers.

4. Conclusion

This paper presented an effective strategy for label-free and highly sensitive detection of CH3L1 and L-FABP, biomarkers of AKI, with GO/Au@Ag core–shell nanoprobes. The GO/Au@Ag substrate possesses the advantages brought by Ag, Au and GO. It is highly-sensitive and stable. The results showed that this method can be used to detect the biomarkers of AKI, CH3L1 and L-FABP, at very low concentrations, 2×10^{-8} mg/mL and 1.2×10^{-8} mg/mL, with wide linear ranges from 2×10^{-1} to 2×10^{-8} mg/mL and 1.2×10^{-1} to 1.2×10^{-8} mg/mL, respectively. The biomarkers can be well quantified to facilitate the early diagnosis of AKI so that patients can be promptly treated to reduce further risk. In addition, the SERS peaks of CH3L1 and L-FABP of very low

concentrations were present simultaneously in the mixed serum solution, demonstrating the feasibility of this method in the real complicated biological environment. The low detection limit showed that the SERS method based on GO/Au@Ag NPs is a reliable method for ultra-sensitive detection of biomarkers. The entire protocol was also convenient, time-saving, and economical. The gold and silver-based substrates also have good biocompatibility, which made them extremely promising in a variety of medical and biotechnology applications.

CRediT authorship contribution statement

Luyao Wang: Investigation, Writing – original draft. **Pei Ma:** Writing – review & editing. **Hui Chen:** Formal analysis, Investigation. **Min Chang:** Investigation. **Ping Lu:** Investigation. **Nan Chen:** Investigation. **Xuedian Zhang:** Investigation. **Yanhua Li:** Investigation. **Mingxing Sui:** Writing – review & editing.

Declaration of Competing Interest

The authors declare that they have no known competing financial interests or personal relationships that could have appeared to influence the work reported in this paper.

Data availability

Data will be made available on request.

References

[1] C. Ronco, R. Bellomo, J.A. Kellum, Acute kidney injury, Lancet 394 (10212) (2019) 1949–1964, https://doi.org/10.1016/s0140-6736(19)32563-2.

[2] E.A. Hoste, et al., Epidemiology of acute kidney injury in critically ill patients: the multinational AKI-EPI study, Intensive Care Med. 41 (8) (2015) 1411–1423, https://doi.org/10.1007/s00134-015-3934-7.

[3] F.B. Lichtenberger, A. Patzak, AKI and CKD, Acta Physiol. (Oxf.) 232 (2) (2021) e13646.

[4] M. Zdziechowska, et al., Serum NGAL, KIM-1, IL-18, L-FABP: new biomarkers in the diagnostics of acute kidney injury (AKI) following invasive cardiology procedures, Int. Urol. Nephrol. 52 (11) (2020) 2135–2143, https://doi.org/10.1007/s11255-020-02530-x.

[5] C. Pontillo, H. Mischak, Urinary biomarkers to predict CKD: is the future in multi-marker panels? Nephrol. Dial. Transplant. 31 (9) (2016) 1373–1375, https://doi.org/10.1093/ndt/gfv467.

[6] T. Bjornsson, Use of serum creatinine concentrations to determine renal function1, Clin. Pharmacokinet. 4 (1979) 200–222, https://doi.org/10.2165/00003088-197904030-00003.

[7] S.S. Waikar, R.A. Betensky, J.V. Bonventre, Creatinine as the gold standard for kidney injury biomarker studies? Nephrol. Dial. Transplant. 24 (11) (2009) 3263–3265, https://doi.org/10.1093/ndt/gfp428.

[8] J.P. Bosch, et al., Renal functional reserve in humans: effect of protein intake on glomerular filtration rate, Am. J. Med. 75 (6) (1983) 943–950, https://doi.org/10.1016/0002-9343(83)90873-2.

[9] P. Amrollahi, et al., Ultra-sensitive automated profiling of EpCAM expression on tumor-derived extracellular vesicles, Front. Genet. 10 (2019) 1273, https://doi.org/10.3389/fgene.2019.01273.

[10] N.M. Selby, et al., An organizational-level program of intervention for AKI: a pragmatic stepped wedge cluster randomized trial, J. Am. Soc. Nephrol. 30 (3) (2019) 505–515, https://doi.org/10.1681/ASN.2018090886.

[11] W. Han, Biomarkers for early detection of acute kidney injury, Curr. Biomark. Find. (2012), https://doi.org/10.2147/cbf.S27898.

[12] K. Kohl, et al., Evaluation of urinary biomarkers for early detection of acute kidney injury in a rat nephropathy model, J. Pharmacol. Toxicol. Methods 105 (2020), 106901, https://doi.org/10.1016/j.vascn.2020.106901.

[13] S.K. Parr, et al., Urinary L-FABP predicts poor outcomes in critically ill patients with early acute kidney injury, Kidney Int. 87 (3) (2015) 640–648, https://doi.org/10.1038/ki.2014.301.

[14] E.A. Hoste, et al., Urinary cell cycle arrest biomarkers and chitinase 3-like protein 1 (CHI3L1) to detect acute kidney injury in the critically ill: a post hoc laboratory analysis on the FINNAKI cohort, Crit. Care 24 (1) (2020) 144, https://doi.org/10.1186/s13054-020-02867-w.

[15] I.J. Yeo, et al., Roles of chitinase 3-like 1 in the development of cancer, neurodegenerative diseases, and inflammatory diseases, Pharmacol. Ther. 203 (2019), 107394, https://doi.org/10.1016/j.pharmthera.2019.107394.

[16] M. Comabella, et al., Chitinase 3-like 1 is not a target antigen in patients with multiple sclerosis, Mult. Scler. 27 (9) (2021) 1455–1457, https://doi.org/10.1177/1352458520980141.

[17] J.h. Leibler, et al., Biomarkers of kidney injury among children in a high-risk region for chronic kidney disease of uncertain etiology, Pediatr. Nephrol. 36 (2) (2021) 387–396, https://doi.org/10.1007/s00467-020-04595-3.

[18] C.P. Walther, J.S. Benoit, Tubular kidney biomarker insights through factor analysis, Am. J. Kidney Dis. 78 (3) (2021) 335–337, https://doi.org/10.1053/j.ajkd.2021.03.016.

[19] I.M. Schmidt, et al., Chitinase-like protein Brp-39/YKL-40 modulates the renal response to ischemic injury and predicts delayed allograft function, J. Am. Soc. Nephrol. 24 (2) (2013) 309–319, https://doi.org/10.1681/ASN.2012060579.

[20] A.L. Conroy, et al., Chitinase-3-like 1 is a biomarker of acute kidney injury and mortality in paediatric severe malaria, Malar. J. 17 (1) (2018) 82, https://doi.org/10.1186/s12936-018-2225-5.

[21] M.A. Ramadan, M. Abdelgwad, M.M. Fouad, Predictive value of novel biomarkers for chronic kidney disease among workers occupationally exposed to silica, Toxicol. Ind. Health 37 (4) (2021) 173–181, https://doi.org/10.1177/0748233721990304.

[22] M.E. Wasung, L.S. Chawla, M. Madero, Biomarkers of renal function, which and when? Clin. Chim. Acta 438 (2015) 350–357, https://doi.org/10.1016/j.cca.2014.08.039.

[23] S.S. Soni, et al., Early diagnosis of acute kidney injury: the promise of novel biomarkers, Blood Purif. 28 (3) (2009) 165–174, https://doi.org/10.1159/000227785.

[24] Maddens, B., et al., Chitinase-like proteins are candidate biomarkers for sepsis-induced acute kidney injury. Mol Cell Proteomics, 2012. 11(6): p. M111 013094. https://doi.org/10.1074/mcp.M111.013094.

[25] J. Peabody, et al., Clinical utility of a biomarker to detect contrast-induced acute kidney injury during percutaneous cardiovascular procedures, Cardiorenal. Med. 12 (1) (2022) 11–19, https://doi.org/10.1159/000520820.

[26] N.R. Jo, K.J. Lee, Y.B. Shin, Enzyme-coupled nanoplasmonic biosensing of cancer markers in human serum, Biosens. Bioelectron. 81 (2016) 324–333, https://doi.org/10.1016/j.bios.2016.03.009.

[27] L. Ma, et al., Development of nanobody-based flow injection chemiluminescence immunoassay for sensitive detection of human prealbumin, Biosens. Bioelectron. 61 (2014) 165–171, https://doi.org/10.1016/j.bios.2014.04.026.

[28] Q. Chen, et al., A novel electrochemical immunosensor based on the rGO-TEPA-PTC-NH(2) and AuPt modified C(6)(0) bimetallic nanoclusters for the detection of Vangl1, a potential biomarker for dysontogenesis, Biosens. Bioelectron. 79 (2016) 364–370, https://doi.org/10.1016/j.bios.2015.12.063.

[29] W.h. Zhang, W. Ma, Y.T. Long, Redox-mediated indirect fluorescence immunoassay for the detection of disease biomarkers using dopamine-functionalized quantum dots, Anal. Chem. 88 (10) (2016) 5131–5136, https://doi.org/10.1021/acs.analchem.6b00048.

[30] J. Ling, Y.F. Li, C.Z. Huang, Visual sandwich immunoassay system on the basis of plasmon resonance scattering signals of silver nanoparticles, Anal. Chem. 81 (4) (2009) 1707.

[31] Y. Higashi, et al., Pharmacokinetic interaction with digoxin and glucocorticoids in rats detected by radio-immunoassay using a novel specific antiserum, Life Sci. 77 (9) (2005) 1055–1067, https://doi.org/10.1016/j.lfs.2005.03.003.

[32] X. Wang, et al., Composition-adjustable Ag-Au substitutional alloy microcages enabling tunable plasmon resonance for ultrasensitive SERS, Chem. Sci. 9 (16) (2018) 4009–4015, https://doi.org/10.1039/c8sc00915e.

[33] Y. He, et al., Metal organic frameworks combining CoFe2O4 magnetic nanoparticles as highly efficient SERS sensing platform for ultrasensitive detection of N-terminal pro-brain natriuretic peptide, ACS Appl. Mater. Interfaces 8 (12) (2016) 7683–7690, https://doi.org/10.1021/acsami.6b01112.

[34] X. Wang, et al., Remarkable SERS activity observed from amorphous ZnO nanocages, Angew. Chem. Int. Ed. Engl. 56 (33) (2017) 9851–9855, https://doi.org/10.1002/anie.201705187.

[35] X. Wang, et al., Two-dimensional amorphous TiO2 Nanosheets enabling high-efficiency photoinduced charge transfer for excellent SERS activity, J. Am. Chem. Soc. 141 (14) (2019) 5856–5862, https://doi.org/10.1021/jacs.9b00029.

[36] J. Zheng, et al., Electrical and SERS detection of disulfide-mediated dimerization in single-molecule benzene-1,4-dithiol junctions, Chem. Sci. 9 (22) (2018) 5033–5038, https://doi.org/10.1039/c8sc00727f.

[37] Y. Sun, et al., Exonuclease III-boosted cascade reactions for ultrasensitive SERS detection of nucleic acids, Biosens. Bioelectron. 104 (2018) 32–38, https://doi.org/10.1016/j.bios.2017.12.047.

[38] F. Huang, et al., High-yield synthesis of hollow octahedral silver nanocages with controllable pack density and their high-performance sers application, Small 12 (39) (2016) 5442–5448, https://doi.org/10.1002/smll.201602280.

[39] H. Abramczyk, et al., Aberrant protein phosphorylation in cancer by using raman biomarkers, Cancers (Basel) 11 (12) (2019), https://doi.org/10.3390/cancers11122017.

[40] C. Liu, et al., Target-triggered regioselective assembly of nanoprobes for Raman imaging of dual cancer biomarkers in living cells, Sens. Actuators B: Chem. (2021) 330, https://doi.org/10.1016/j.snb.2020.129319.

[41] X. Ling, et al., Can graphene be used as a substrate for Raman enhancement? Nano Lett 10 (2) (2010) 553–561, https://doi.org/10.1021/nl903414x.

[42] L. Zhang, et al., Enhanced chemotherapy efficacy by sequential delivery of siRNA and anticancer drugs using PEI-grafted graphene oxide, Small 7 (4) (2011) 460–464, https://doi.org/10.1002/smll.201001522.

[43] H. Zhang, et al., Insights into the binding mechanism of two-dimensional black phosphorus nanosheets-protein associations, Spectrochim Acta A Mol Biomol Spectrosc 227 (2020), 117662, https://doi.org/10.1016/j.saa.2019.117662.

[44] G. Frens, Controlled Nucleation for the Regulation of the Particle Size in Monodisperse Gold Suspensions, Nat. Phys. Sci. 241 (105) (1973) 20–22, https://doi.org/10.1038/physci241020a0.

[45] BMC Nephrol. 15 (1) (2014) 133.

[46] J.h. Lee, et al., Clinical implication of plasma and urine YKL-40, as a proinflammatory biomarker, on early stage of nephropathy in type 2 diabetic patients, J Diabetes Complications 26 (4) (2012) 308–312, https://doi.org/10.1016/j.jdiacomp.2012.04.012.

[47] E. Sato, et al., Urinary excretion of liver-type fatty acid-binding protein reflects the severity of sepsis. Renal Replacement, Therapy 3 (1) (2017), https://doi.org/10.1186/s41100-017-0107-x.

[48] A. Simsek, V. Tugcu, A.I. Tasci, New biomarkers for the quick detection of acute kidney injury, ISRN Nephrol 2013 (2013), 394582, https://doi.org/10.5402/2013/394582.

[49] L. Wang, et al., Rapid Determination of Mixed Pesticide Residues on Apple Surfaces by Surface-Enhanced Raman Spectroscopy, Foods 11 (8) (2022), https://doi.org/10.3390/foods11081089.

[50] P. Ma, et al., Rapid quantitative determination of chlorpyrifos pesticide residues in tomatoes by surface-enhanced Raman spectroscopy, European Food Research and Technology 246 (1) (2019) 239–251, https://doi.org/10.1007/s00217-019-03408-8.

[51] T. Vo-Dinh, et al., Rational engineering of highly sensitive SERS substrate based on nanocone structures. 7673 (2010) 76730O, https://doi.org/10.1117/12.849959.

[52] G.L. Long, J.D. Winefordner, Limit of Detection A Closer Look at the IUPAC Definition, Anal. Chem. 55 (07) (1983) 712A–724A, https://doi.org/10.1021/ac00258a724.

[53] L. Kong, J. Chen, M. Huang, GO/Au@Ag nanobones decorated membrane for simultaneous enrichment and on-site SERS detection of colorants in beverages, Sens. Actuators B: Chem. (2021) 344, https://doi.org/10.1016/j.snb.2021.130163.

[54] G. Ding, et al., Graphene oxide-silver nanocomposite as SERS substrate for dye detection: Effects of silver loading amount and composite dosage, Appl. Surf. Sci. 345 (2015) 310–318, https://doi.org/10.1016/j.apsusc.2015.03.175.

[55] J. Zhu, et al., SERS detection of glucose using graphene-oxide-wrapped gold nanobones with silver coating, J. Mater. Chem. C 7 (11) (2019) 3322–3334, https://doi.org/10.1039/c8tc05942j.

[56] Y. Sun, et al., In situ synthesis of graphene oxide/gold nanocomposites as ultrasensitive surface-enhanced Raman scattering substrates for clenbuterol detection, Anal. Bioanal. Chem. 412 (1) (2019) 193–201, https://doi.org/10.1007/s00216-019-02230-1.

[57] H. Fang, et al., Ultrasensitive and quantitative detection of paraquat on fruits skins via surface-enhanced Raman spectroscopy, Sens. Actuators B: Chem. 213 (2015) 452–456.

[58] M. Manciu, et al., Assessment of renal osteodystrophy via computational analysis of label-free Raman detection of multiple biomarkers, Diagnostics (Basel) 10 (2) (2020), https://doi.org/10.3390/diagnostics10020079.

[59] P.E. Prevelige, et al., Subunit conformational changes accompanying bacteriophage P22 capsid maturation, Biochemistry 32 (2) (1993) 537–543, https://doi.org/10.1021/bi00053a019.

[60] L. Ashton, et al., Detection of glycosylation and iron-binding protein modifications using Raman spectroscopy, Analyst 142 (5) (2017) 808–814, https://doi.org/10.1039/c6an02516a.

[61] Vohník, S., et al., Conformation, stability, and active-site cysteine titrations of Escherichia coli D26A thioredoxin probed by Raman spectroscopy. Protein science : a publication of the Protein Society, 1998. 7(1): p. 193-200. https://doi.org/10.1002/pro.5560070120.

[62] Y. Hu, et al., Rapid and sensitive detection of NGAL for the prediction of acute kidney injury via a polydopamine nanosphere/aptamer nanocomplex coupled with DNase I-assisted recycling amplification, Analyst 145 (10) (2020) 3620–3625, https://doi.org/10.1039/d0an00474j.

[63] J. Liang, et al., Measurement of urinary matrix metalloproteinase-7 for early diagnosis of acute kidney injury based on an ultrasensitive immunomagnetic microparticle-based time-resolved fluoroimmunoassay, Clin. Chim. Acta 490 (2019) 55–62, https://doi.org/10.1016/j.cca.2018.11.037.

[64] Y.J. Hwang, et al., Acute kidney injury after using contrast during cardiac catheterization in children with heart disease, J. Korean Med. Sci. 29 (8) (2014) 1102–1107, https://doi.org/10.3346/jkms.2014.29.8.1102.

[65] T. Sun, et al., Rapid and sensitive detection of L-FABP for prediction and diagnosis of acute kidney injury in critically ill patients by chemiluminescent immunoassay, J. Clin. Lab. Anal. 35 (11) (2021) e24051.

[66] D.S. Cooper, et al., Follow-up renal assessment of injury long-term after acute kidney injury (FRAIL-AKI), Clin. J. Am. Soc. Nephrol. 11 (1) (2016) 21–29, https://doi.org/10.2215/CJN.04240415.

[67] L. Amaral Pedroso, et al., Acute kidney injury biomarkers in the critically ill, Clin. Chim. Acta 508 (2020) 170–178, https://doi.org/10.1016/j.cca.2020.05.024.

[68] H. Chen, et al., Simultaneous and ultra-sensitive SERS detection of SLPI and IL-18 for the assessment of donor kidney quality using black phosphorus/gold nanohybrids, Opt. Express 30 (2) (2022) 1452–1465, https://doi.org/10.1364/OE.445809.

[69] Y. Yuan, et al., Rapid detection of illegally added Nifedipine in Chinese traditional patent medicine by surface-enhanced Raman spectroscopy, Anal. Sci. (2021), https://doi.org/10.2116/analsci.21P148.